NATIONAL TRANSPORTATION SAFETY BOARD
Office of Research and Engineering
Vehicle Performance Division
Washington, D.C. 20594

April 23, 2015

FINITE ELEMENT MODELING STUDY REPORT

A. ACCIDENT INFORMATION

Place	:	Casselton, North Dakota
Date	:	December 30, 2013
Vehicle	:	BNSF Grain Freight Car, G-RYLRGT9-26A
NTSB No.	:	DCA14MR004
Investigator	:	Richard Hipskind

B. TOPICS ADDRESSED

Finite element modeling to examine local stress concentration due to void defect in wheelset axle.

C. DETAILS OF THE STUDY

A 3D finite element model of the accident train axle assembly was constructed based on drawings and 3D laser scan data. Loads corresponding to design loads were applied to the structure, as well as boundary conditions simulating wheel-rail interaction. Multiple bending directions were analyzed to identify the worst-case scenario in terms of local stress concentration. Both the cases with and without the internal void defect were analyzed, and the results were compared to show the effect of the defect on local stress concentration. The finite element modeling was carried out using Abaqus 6.14-1.

1. Geometry

a. The wheelset

The finite element model of the wheelset contained the axle and the two mounted wheels. The wheelset in the accident train was identified to have an AAR Class K (6 ½ x 9) axle and 36-inch, AAR 1-B, wide flange wheels [Reference 1]. The axle finite element model was created based on the AAR standard [Reference 2], as well as the drawing shown in figure 1. The wheel model was created based on the AAR standard [Reference 2] with simplified straight flanges. Figures 2 and 3 show the isometric and plan view of the created axle assembly model in Abaqus/CAE.

b. The void defect

Investigation of the fractured axle revealed an internal void defect. The fractured axle was sectioned and scanned using a FaroArm 3D scanner. The point cloud data from the scan was first converted to smooth 3D surfaces using Geomagic Studio and

then imported into Abaqus/CAE to create a 3D model of the axle with the internal defect. Figure 4 shows the surfaces composing the internal defect, and figure 5 shows the section view of the axle with the internal defect visible. The relative position of the void in the longitudinal direction was determined based on measurement [Reference 3] and is shown in figure 6. The orientation of the void would rotate with the axle. A view of the void in the cross-section plane is shown in figure 7. Some characteristic dimensions of the axle and the void are also shown in figures 6 and 7.

2. Material properties

Both the axle and the wheels were made of carbon steel. Only elastic properties were needed for the purpose of this study. Specifically, Young's modulus for carbon steel was taken as 29,000 ksi, and Poisson's ratio was taken as 0.3.

3. Mesh

The axle was meshed with quadratic tetrahedral elements (C3D10 in Abaqus). Tetrahedral elements were necessary for meshing the irregular geometry of the axle with internal defect. The wheels were meshed with linear reduced integration brick elements (C3D8R). The wheels only required a coarse mesh as deformation of the wheel was not of interest for this study. Figures 8 and 9 show the finite element mesh on the global structure and in the vicinity of the void defect. Mesh resolution increased considerably in order to capture the complex geometry associated with the void defect. The mesh statistics are summarized in Table 1 and show the increased model size with the internal defect modeled. Mesh convergence studies were performed for both models, and the mesh size presented was chosen based on both accuracy and efficiency.

Table 1. Mesh statistics

Model	Total Number of Elements	Typical Mesh Dimension	Smallest Mesh Dimension
Without Defect	102,830	0.7 inch	0.7 inch
With Defect	252,027	0.7 inch	0.03 inch

4. Loads and boundary conditions

Two types of loading were considered based on published studies [References 5 and 6]. The first load is a vertical force of 35,750 lbs evenly distributed on the journal surfaces on both ends of the axle. This load represents the gross rail load (GRL) of 286,000 lbs. The second load is a lateral force of 8,000 lbs distributed over the axle end face. This load represented curving forces in service [Reference 4]. The two loads were applied to the structure in two separate loading steps. The load associated with the wheel press fit on the axle was not included in the analysis since the wheelseat region was not of primary interest of this study. Instead, the wheel was rigidly constrained to

the axle at the wheelseat. Figure 10 shows the graphic representation of the applied loads.

The wheels were constrained in a way to simulate wheel-track interaction. Specifically, contact between wheel and track was approximated to a point at the bottom of the wheel, where the structure is constrained for vertical motion. One wheel was also constrained horizontally at the bottom flange to resist the applied lateral force. The wheels were allowed to rotate as a result of the bending of the axle. This approximation did not account for the more complex aspects of wheel-track interaction, such as finite contact area and relative sliding, but was sufficient for the current study focusing on the axle. The structure was also constrained for the rigid body motion of wheel spinning. Figure 11 illustrates the applied boundary conditions.

For the case without the internal defect, the structure was rotationally symmetric with respect to the longitudinal axis, and hence it was sufficient for this analysis to consider only one bending direction. For the case with the internal defect, the symmetry was lost and different bending directions needed to be analyzed. Eight bending scenarios were analyzed in this study, and the associated bending directions are shown in figure 12. The angle that was used to identify the directions was measured counterclockwise from the negative global z-direction of the model. For each bending scenario the load and support location were rotated about the axle axis accordingly.

5. Output

The case without the internal defect was analyzed first. Figure 13 shows the deformed axle assembly with deformation magnified 50 times for better visualization. Figure 14 and 15 show the contours of the Mises stress and the bending stress (σ_{yy} component), respectively. Peak stress was observed at the inboard journal fillet on the side of the lateral load, and the peak tensile stress was about 14.3 ksi in magnitude. Both the deformed shape and the stress distribution were consistent with that of a bent axle with simple supports at wheel locations. The stress distribution and magnitude were also consistent with what is reported in Reference 5.

The case with the internal defect was analyzed next. The previously mentioned 8 bending scenarios were analyzed sequentially. Figure 16 and 17 show the cut view of the Mises stress contour plot of the 0-degree bending case. Figures 18 and 19 plot the same stress of the same case on the void surface. Figures 20 through 23 show the corresponding bending stress contours. Local stress exceeding 17.5 ksi, shown in red, can be found on the “ridge” of the surface furthest away from the bending neutral axis, and the peak value for Mises stress was approximately 26.3 ksi, which is nearly twice as large as the peak Mises stress found in the case without the internal defect. The 17.5 ksi value was taken from Reference 5, which cited a previous AAR experimental study that determined a stress level exceeding 17.5 ksi could cause fatigue failure in axles.

Figures 24 and 25 show the Mises stress contour on the void surface overlaid from all 8 bending cases, where maximum stress values from all 8 bending cases are shown in a single plot. The same 17.5 ksi threshold was used for the plot legend.

Figures 26 and 27 show the same overlaid plot for the maximum principal stress contour. It can be seen that the region with high stress extends when all 8 bending directions are considered but is still limited to the “ridge” of the void surface. The high stress region is highlighted in figure 28 for better visualization. For comparison, figure 29 [Figure 8 of Reference 3] shows the actual fracture surface of the broken axle with progressive and overstress areas labeled. The area of progressive fatigue cracking was consistent with the high stress region shown in figure 28.

6. Summary

The finite element modeling described in this study shows that the observed internal defect could cause a local stress that is significantly higher than the bending stress on the axle surface under the load cases investigated, and the magnitude of that local stress can be higher than 17.5 ksi, which according to Reference 4 can lead to fatigue failure. In addition, the region where high stresses were observed was consistent with where the fatigue cracks originated in the accident axle.

It should be noted that the region of the void surface where high stresses were observed had high curvature and hence required a very dense mesh to accurately capture the local stress field. This was further complicated by the fact that the modeled axle fractured in two halves and the surfaces created from scan data needed to be stitched at the fracture surface, which made the geometry at the jointed interface less precise. For these reasons, the value of the predicted peak stress was only approximate, but the peak stress is still expected to occur in the same place along the void surface, and the stress level would still be expected to exceed the 17.5 ksi threshold in Reference 4.

D. REFERENCES

1. Mechanical Group Factual Report, Accident DCA14MR004, National Transportation Safety Board, Washington, DC, 2014.
2. Association of American Railroads, Manual of Standard and Recommended Practices, Wheels and Axles Manual, 2011.
3. Materials Laboratory Factual Report 14-055, Accident DCA14MR004, National Transportation Safety Board, Washington, DC, 2014.
4. C.P. Lonsdale, B.T. Tusa, and S.L. Dedmon, Radial Ultrasonic Testing of Freight Car Axles, ASME/IEEE Joint Rail Conference & Internal Combustion Engine Spring Technical Conference, Pueblo, CO, 2007.
5. C.P. Lonsdale, G.E. Dahlman, S.L. Dedmon, J.M. Pilch, and J.M. Galbraith, Continuing Efforts to Improve Axle Performance in Heavy haul Service, 15th International Wheelset Congress, Prague, Czech Republic, 2007.

Xiaohu Liu
Finite Element Analyst

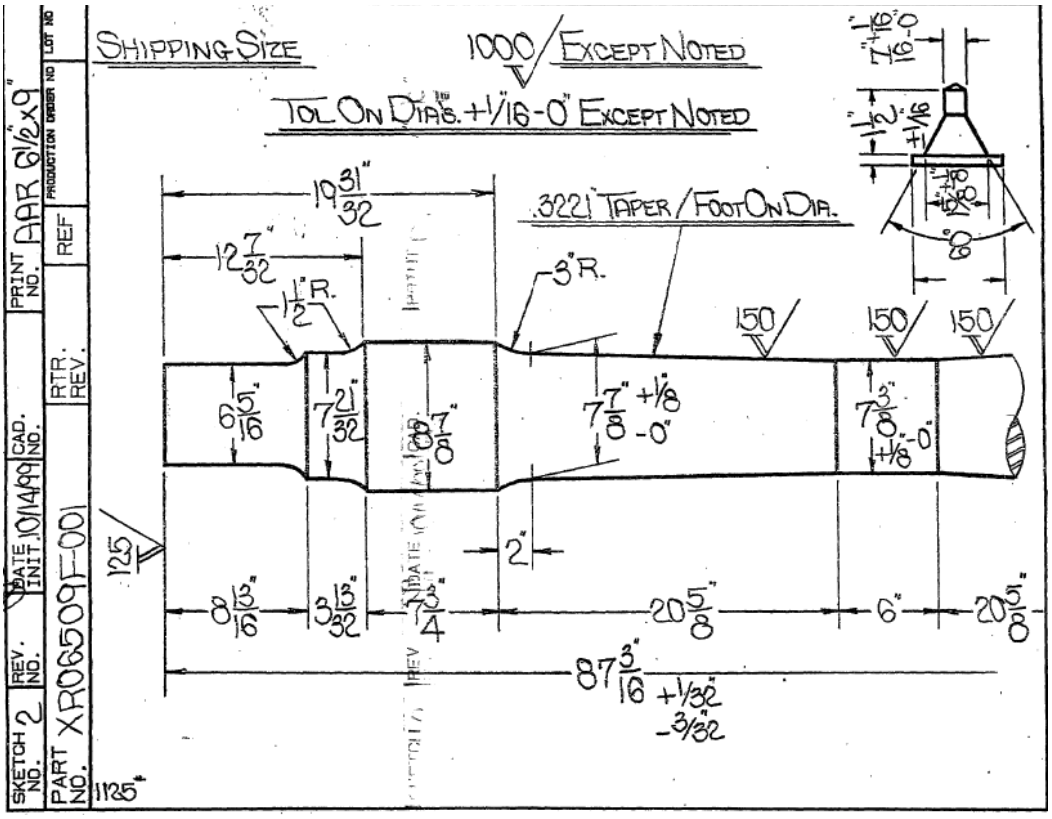

Figure 1. Axle design drawing.

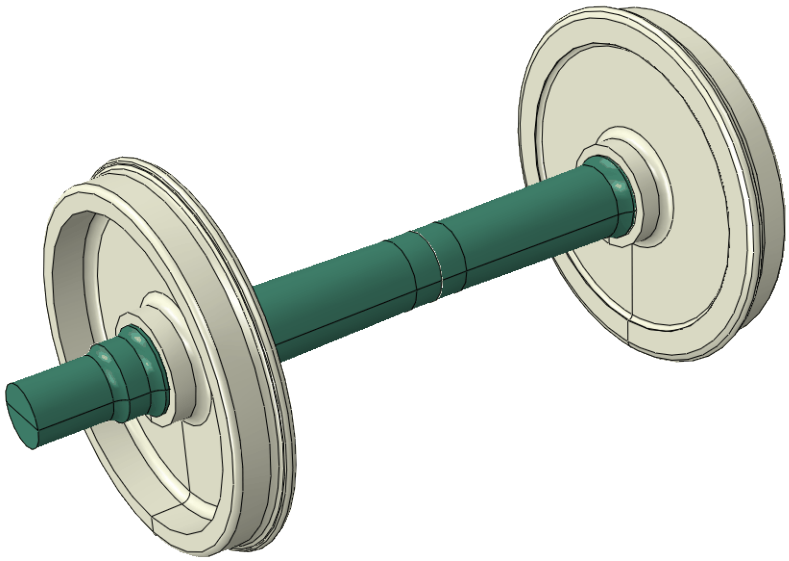

Figure 2. Created geometry of the wheelset, isometric view.

Figure 3. Created geometry of the wheelset, plan view.

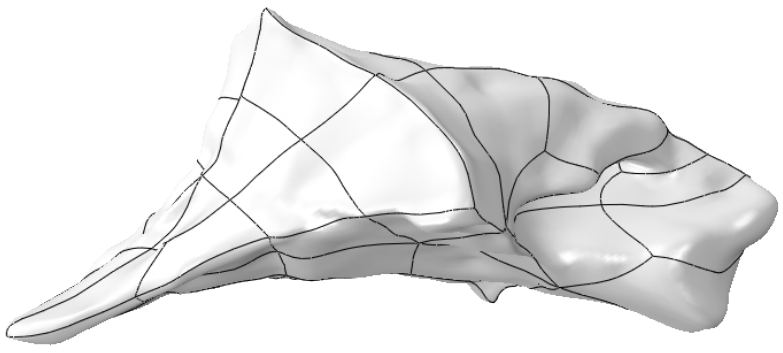

Figure 4. Surfaces of the internal void defect.

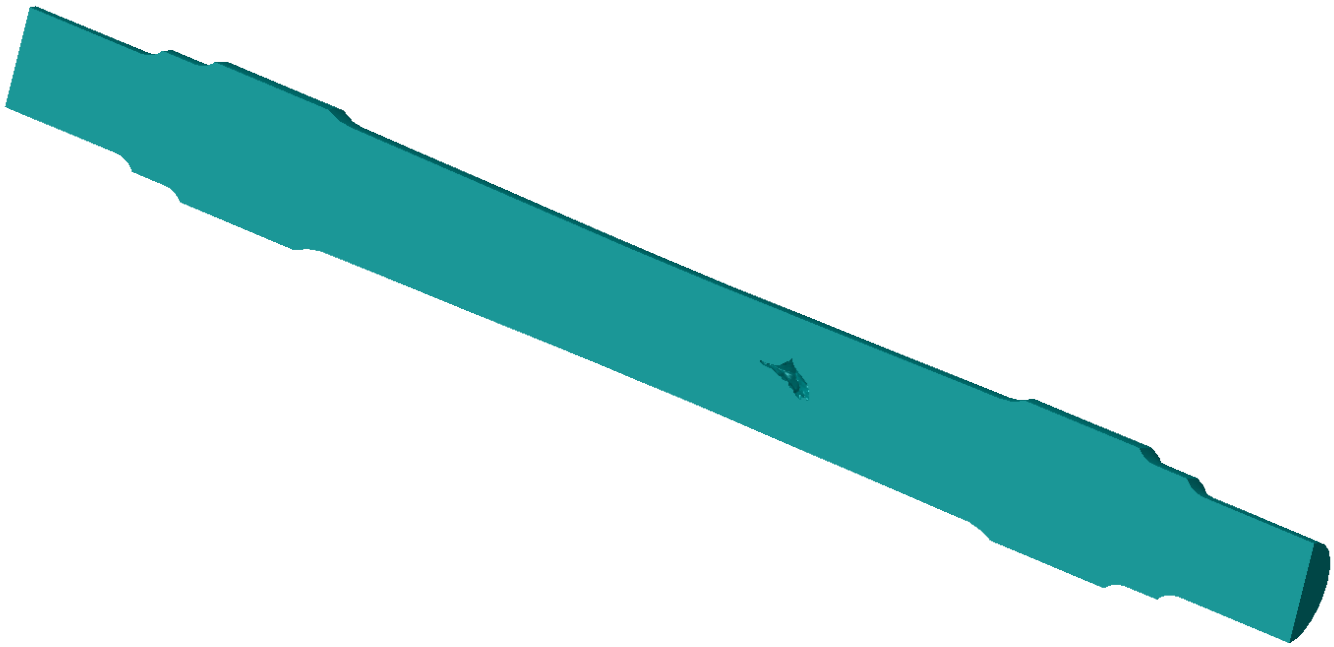

Figure 5. The geometry of the axle with the internal void defect.

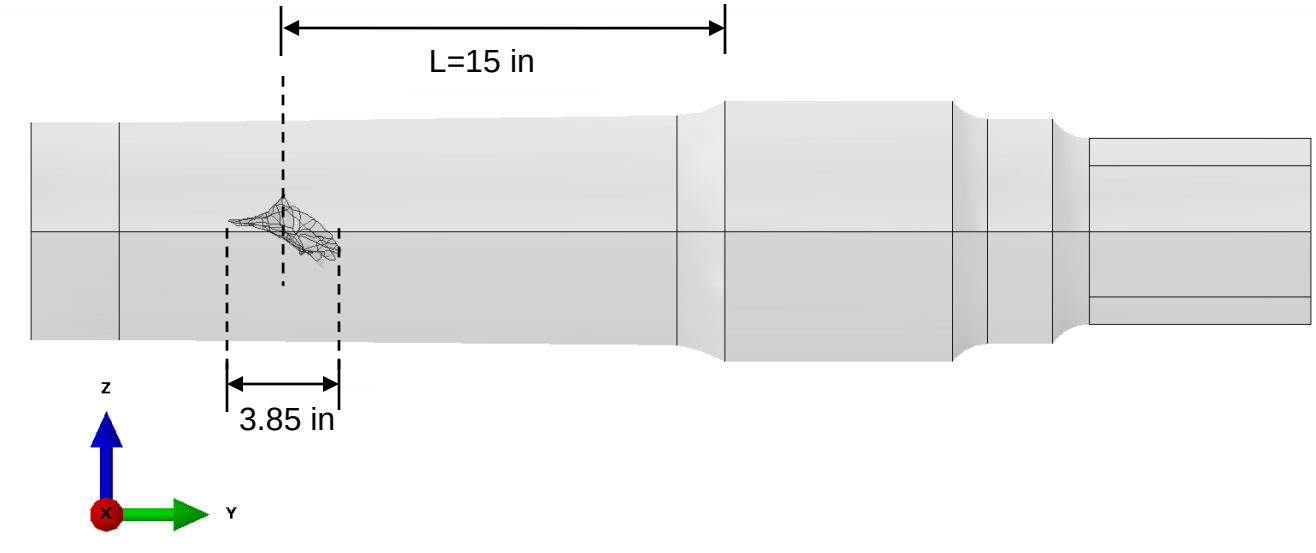

Figure 6. Positioning of the void within the axle, longitudinal view.

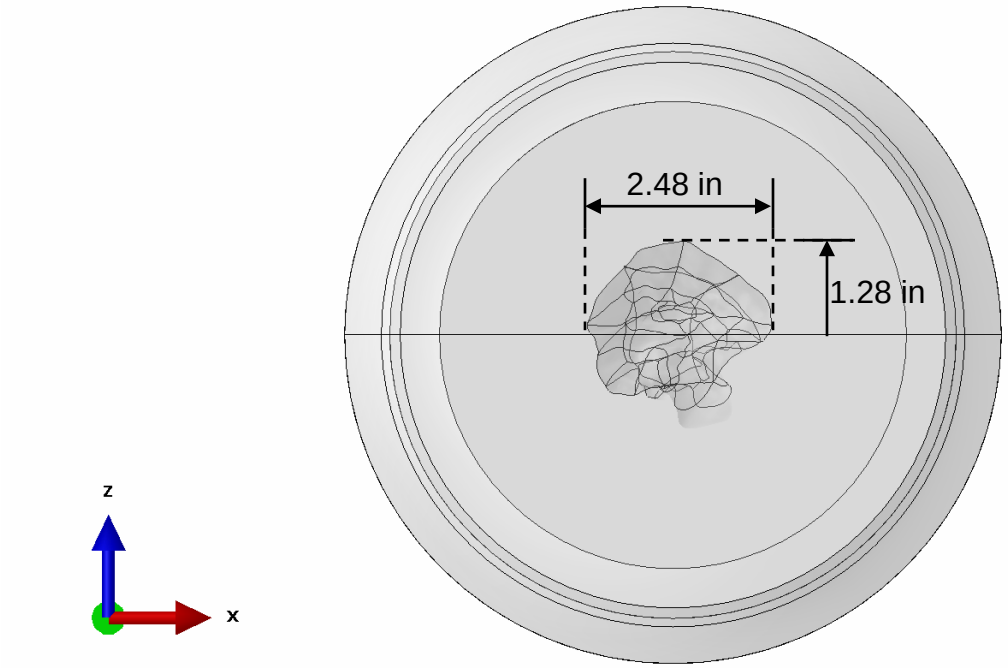

Figure 7. Positioning of the void within the axle, cross-section view.

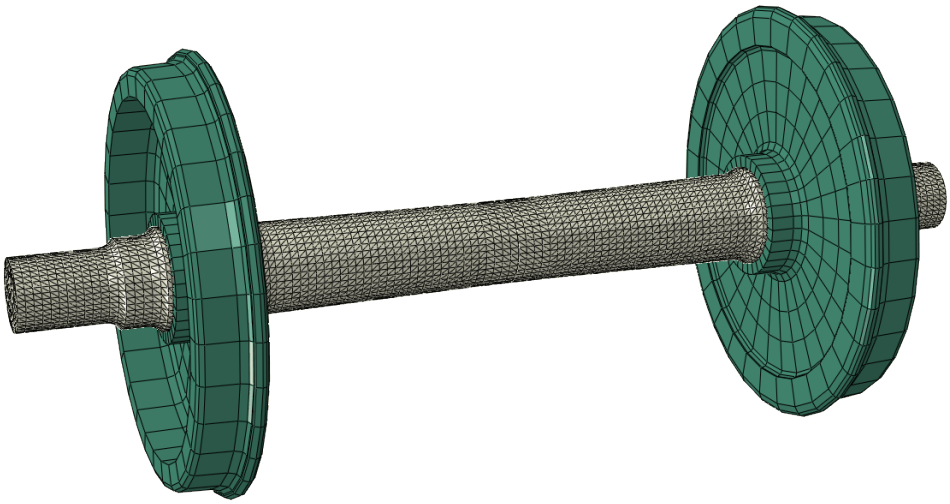

Figure 8. Finite element mesh of the wheelset model.

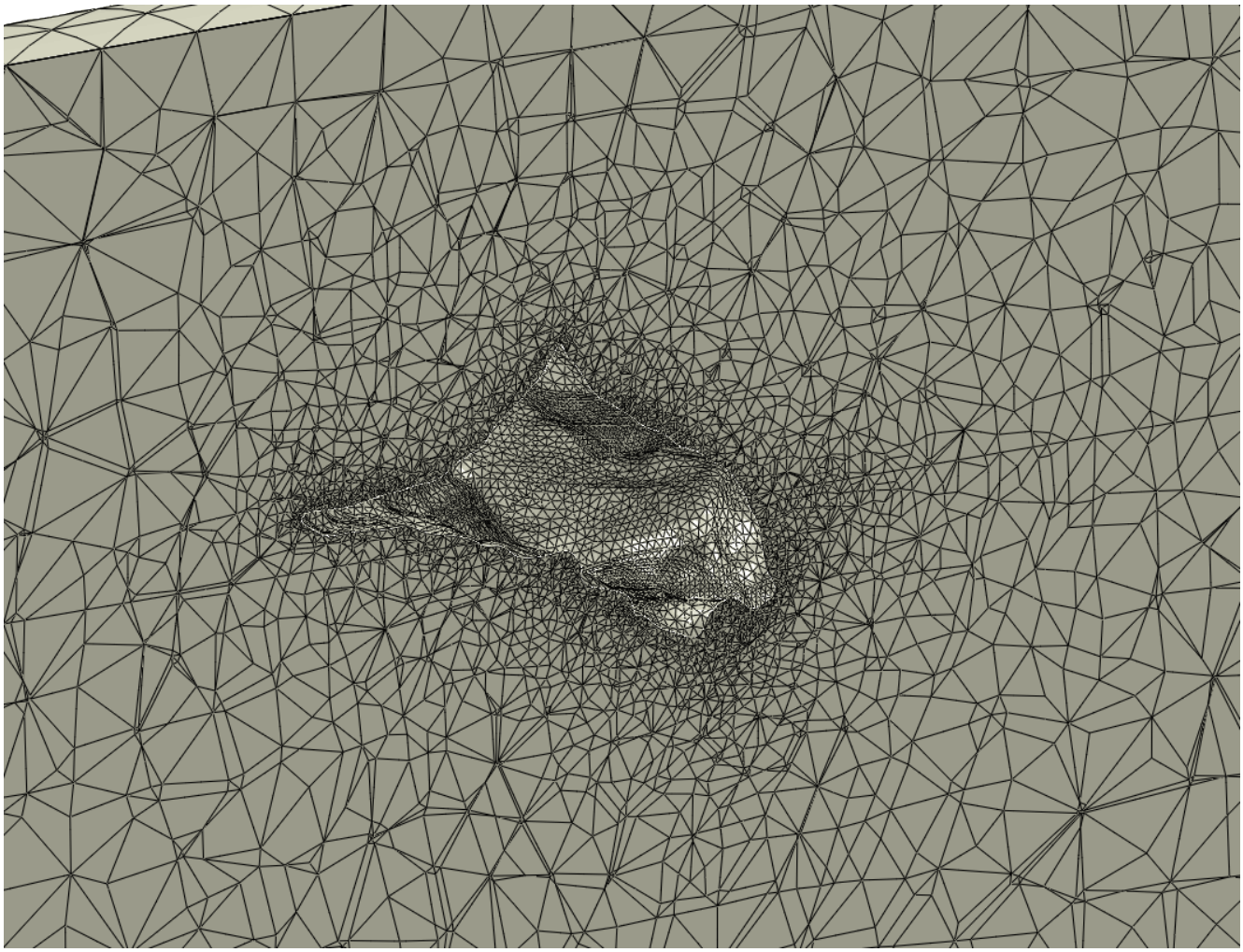

Figure 9. Mesh detail in the vicinity of the void defect.

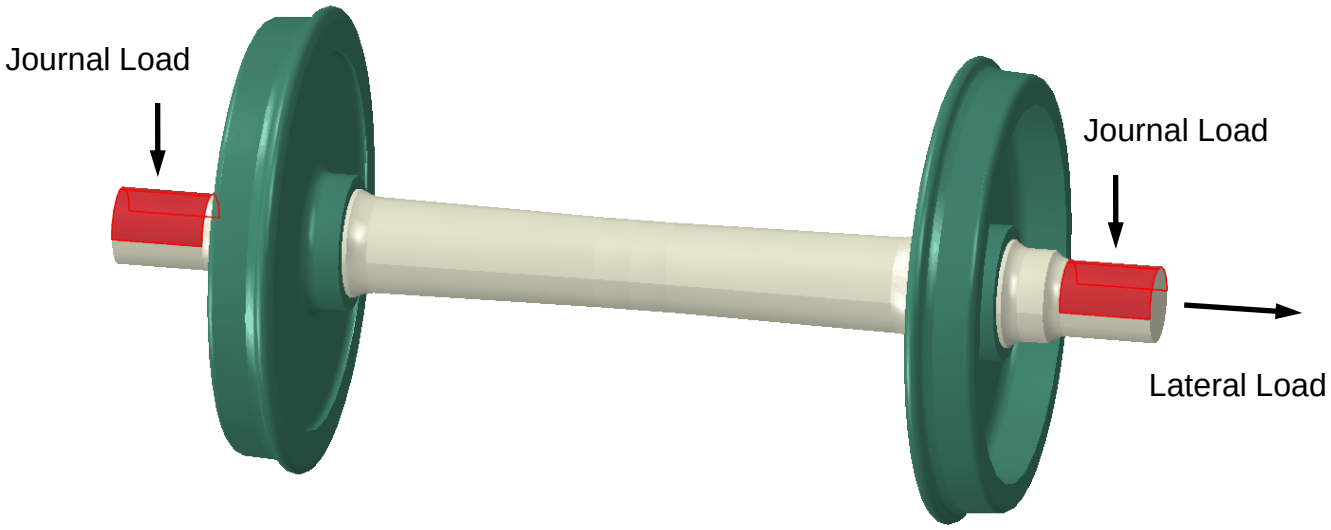

Figure 10. Applied loads to the wheelset.

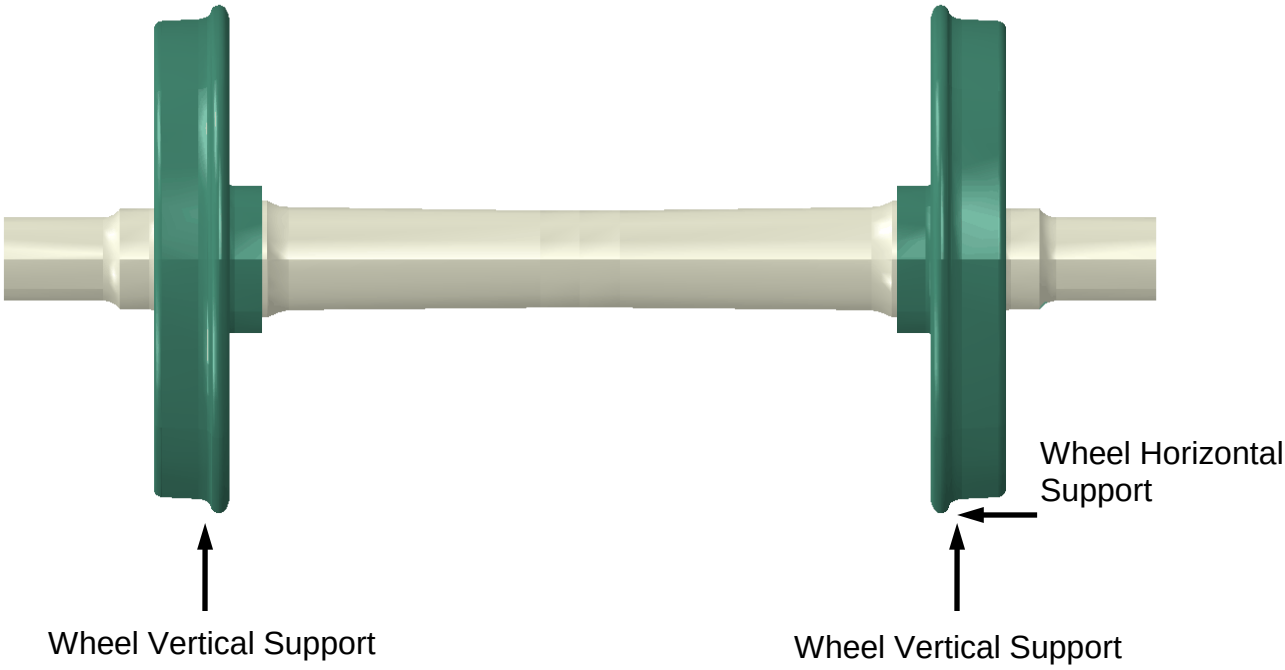

Figure 11. Boundary conditions on the wheelset.

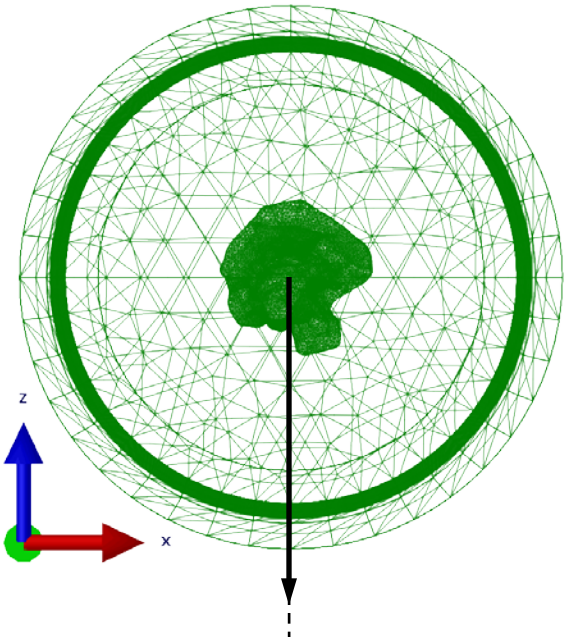

0°

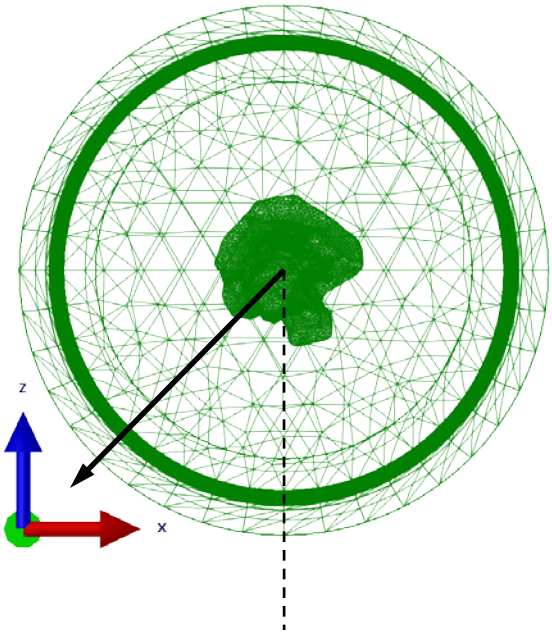

45°

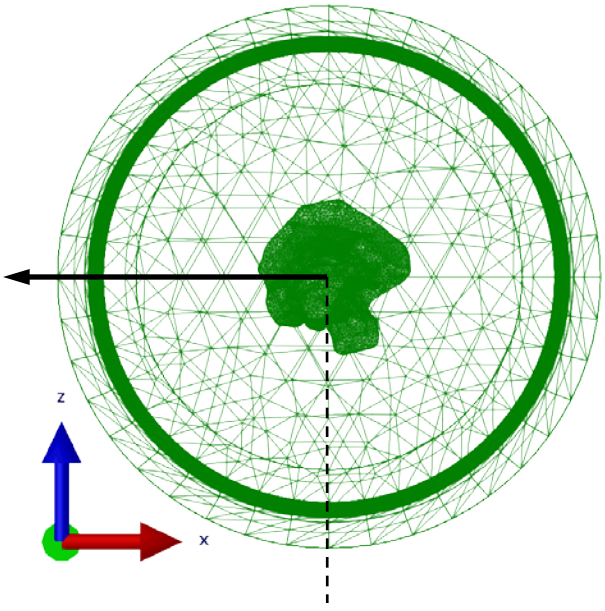

90°

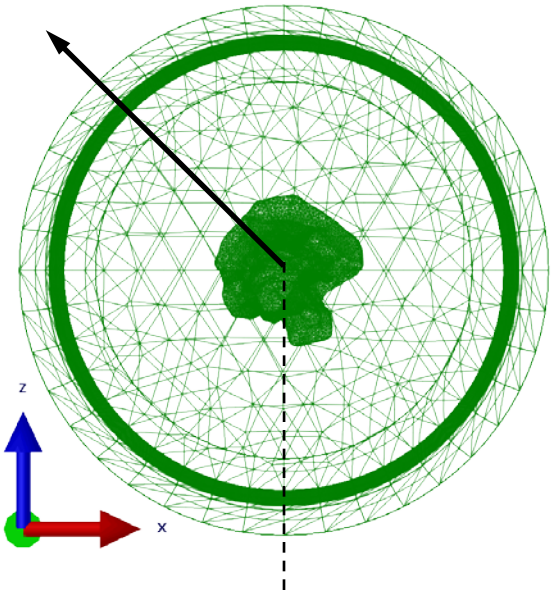

135°

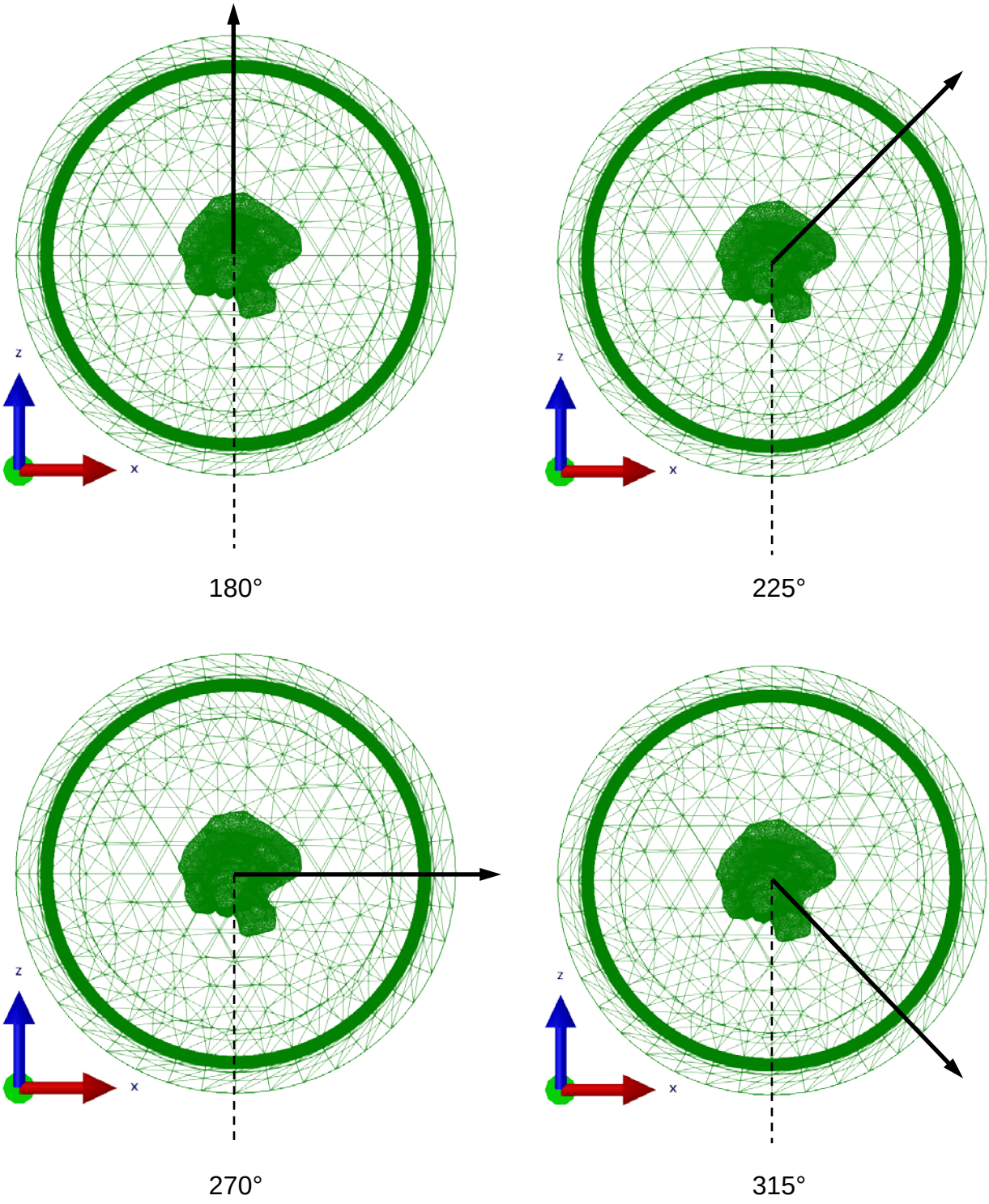

Figure 12. The 8 analyzed bending scenarios.

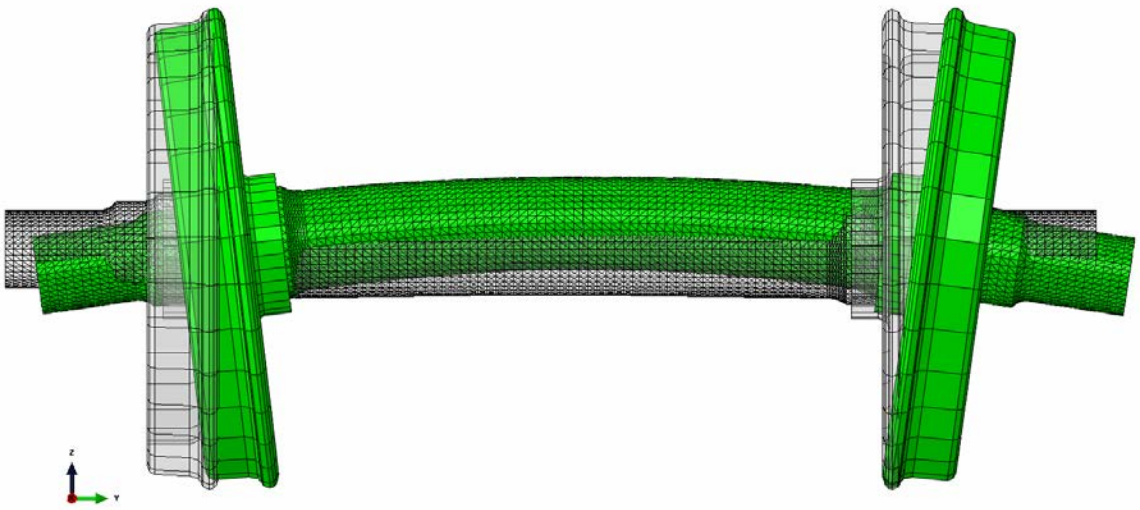

Figure 13. Deformed shape of the bent wheelset, deformation magnified 50 times.

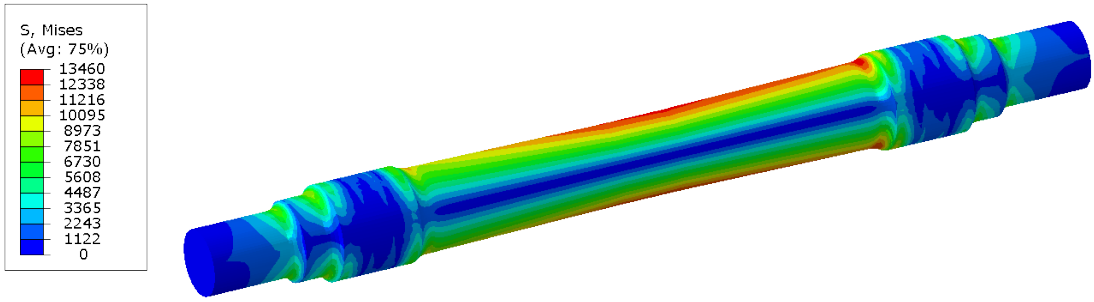

Figure 14. Contours of Mises stress (unit: psi) on the axle, for the case without internal defect.

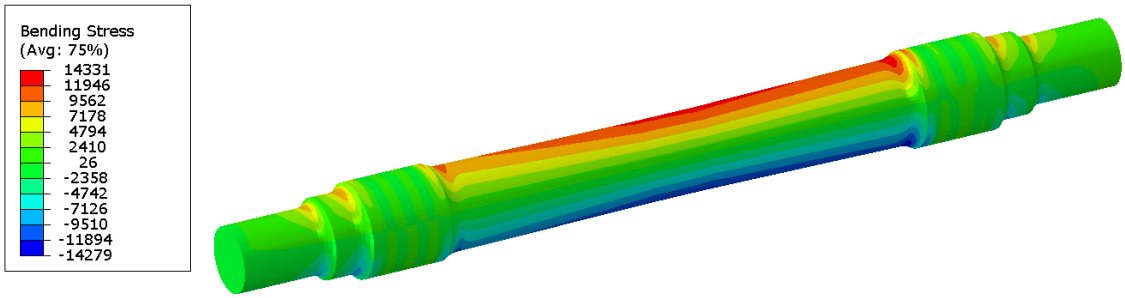

Figure 15. Contours of bending stress (unit: psi) on the axle, for the case without internal defect.

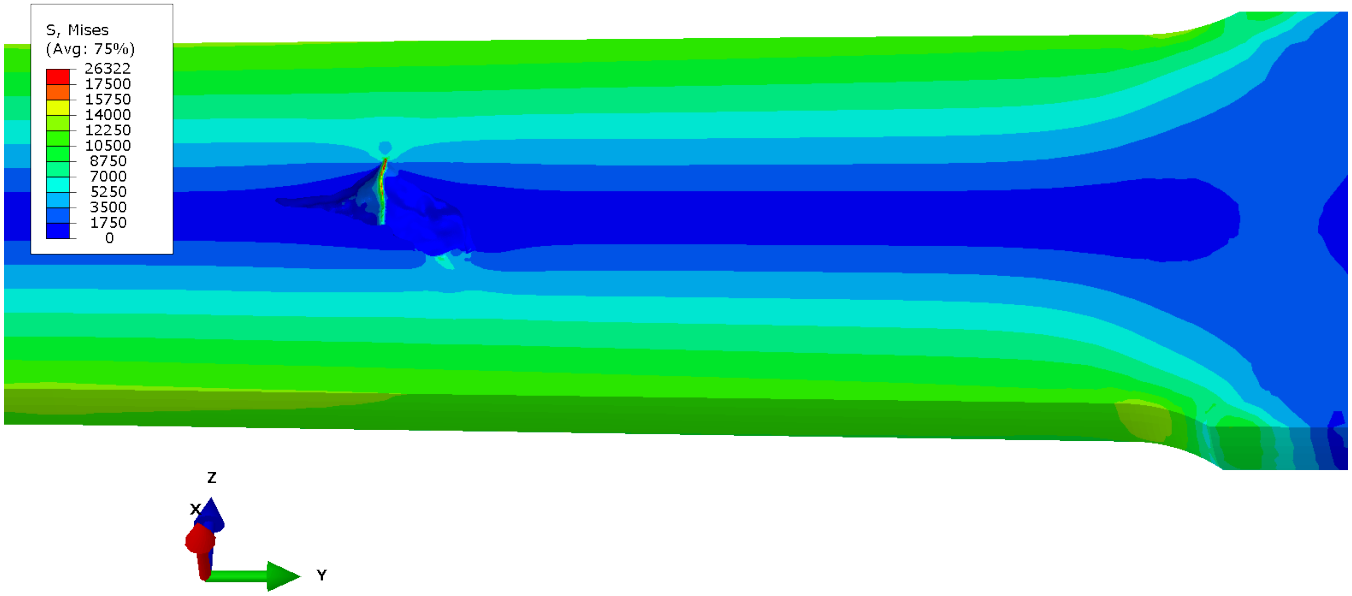

Figure 16. Longitudinal oblique cut view of Mises stress (unit: psi) contour of 0-degree bending case.

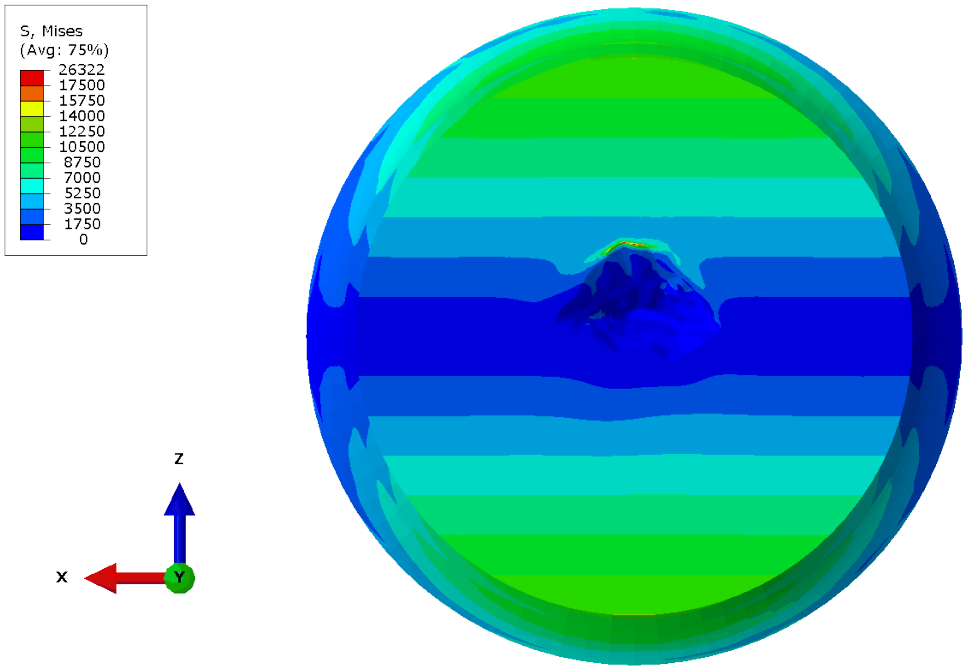

Figure 17. Cross-sectional view of Mises stress (unit: psi) contour of 0-degree bending case.

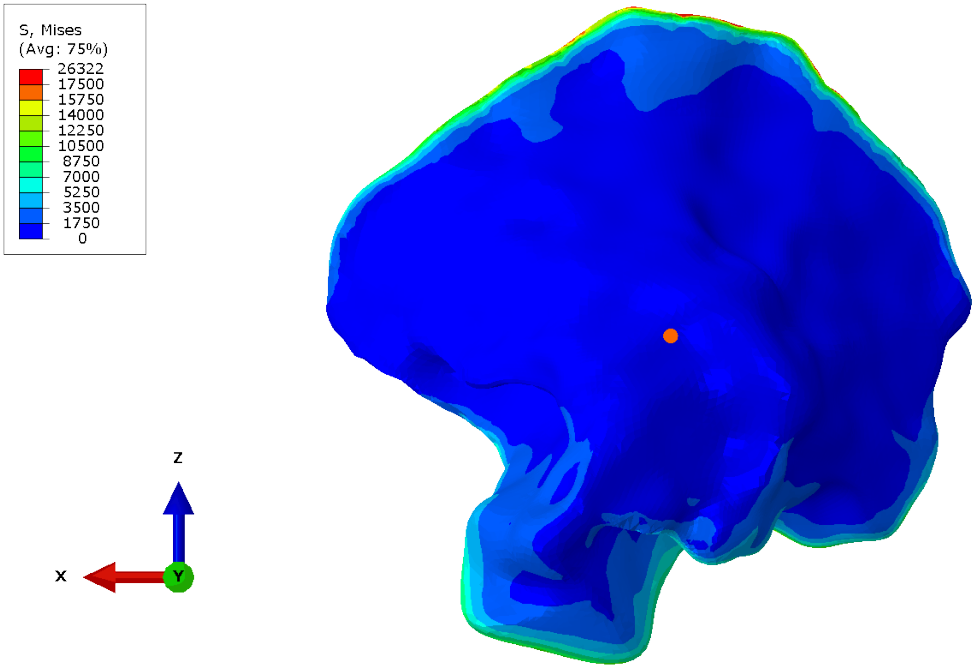

Figure 18. Mises stress (unit: psi) contour on the void surface, 0-degree bending case, end view, with axle centerline location marked.

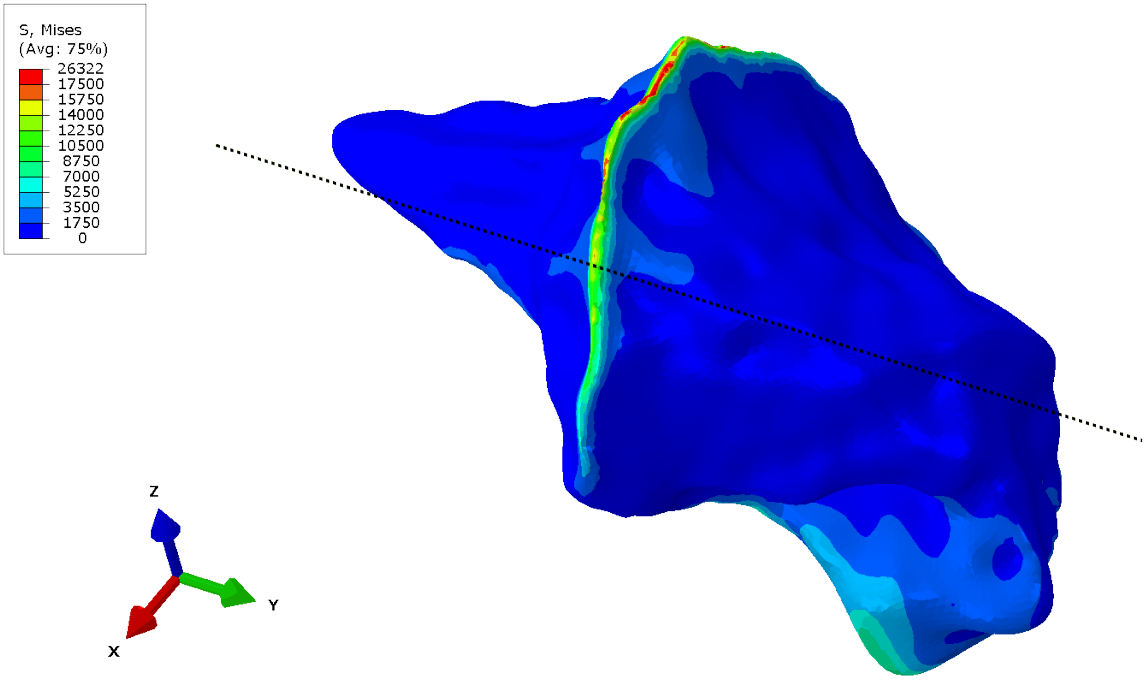

Figure 19. Mises stress (unit: psi) contour on the void surface, 0-degree bending case, isometric view, with axle centerline shown.

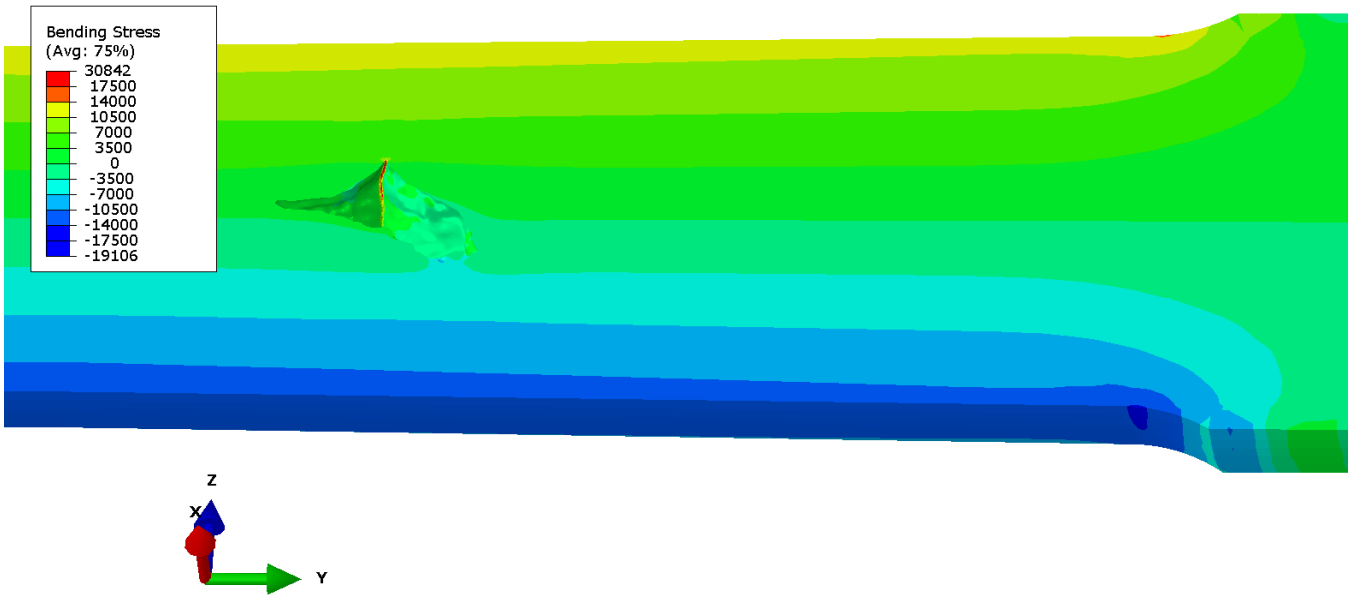

Figure 20. Longitudinal oblique cut view of bending stress (unit: psi) contour of 0-degree bending case.

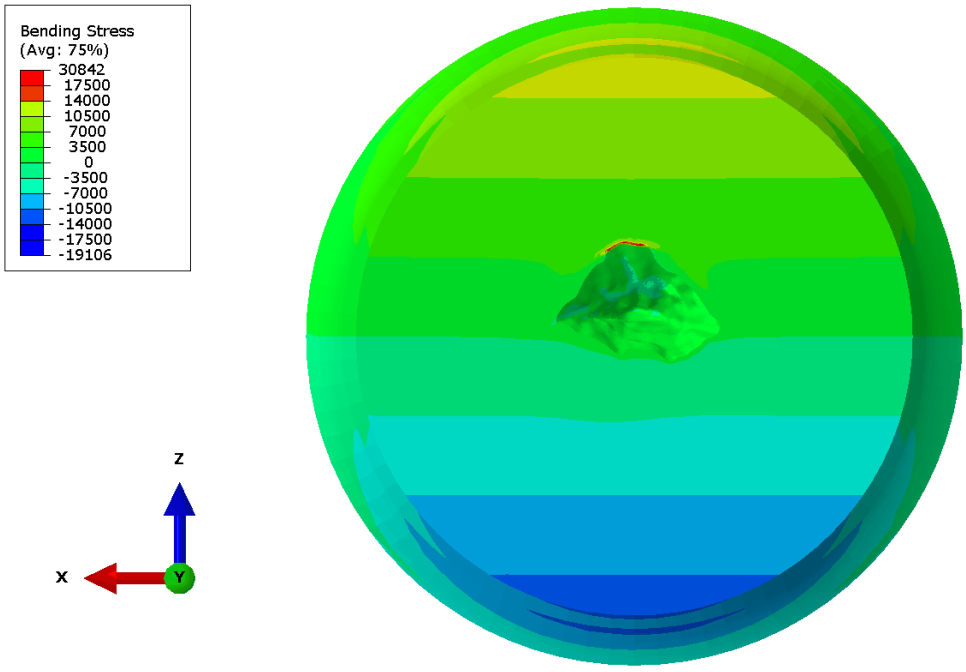

Figure 21. Cross-sectional view of bending stress (unit: psi) contour of 0-degree bending case.

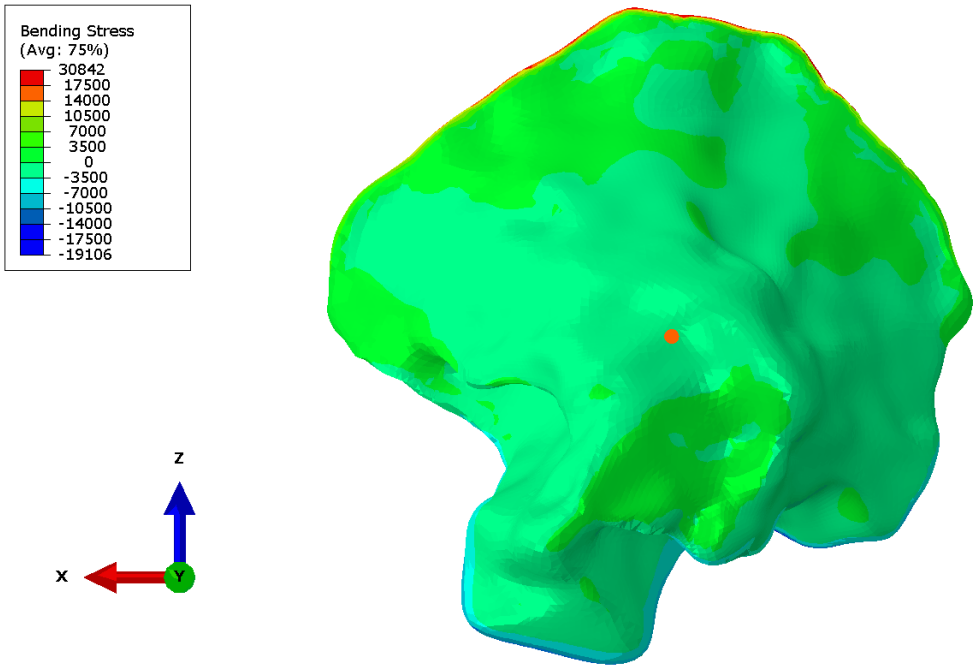

Figure 22. Bending stress (unit: psi) contour on the void surface, 0-degree bending case, end view, with axle centerline location marked.

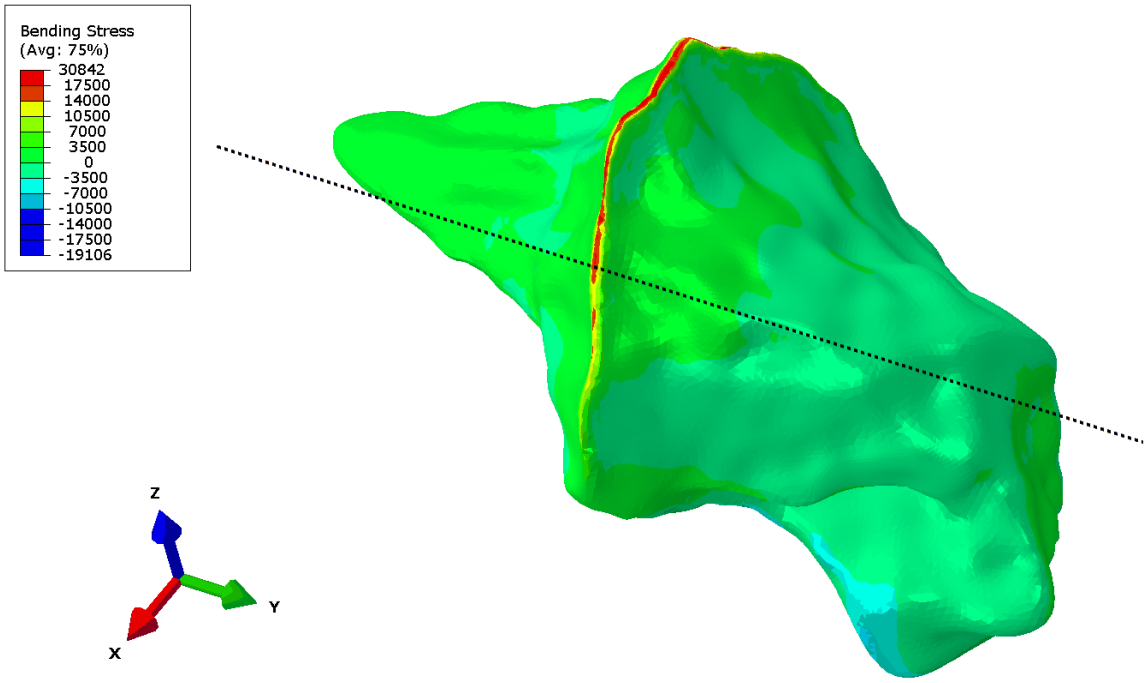

Figure 23. Bending stress (unit: psi) contour on the void surface, 0-degree bending case, isometric view, with axle centerline shown.

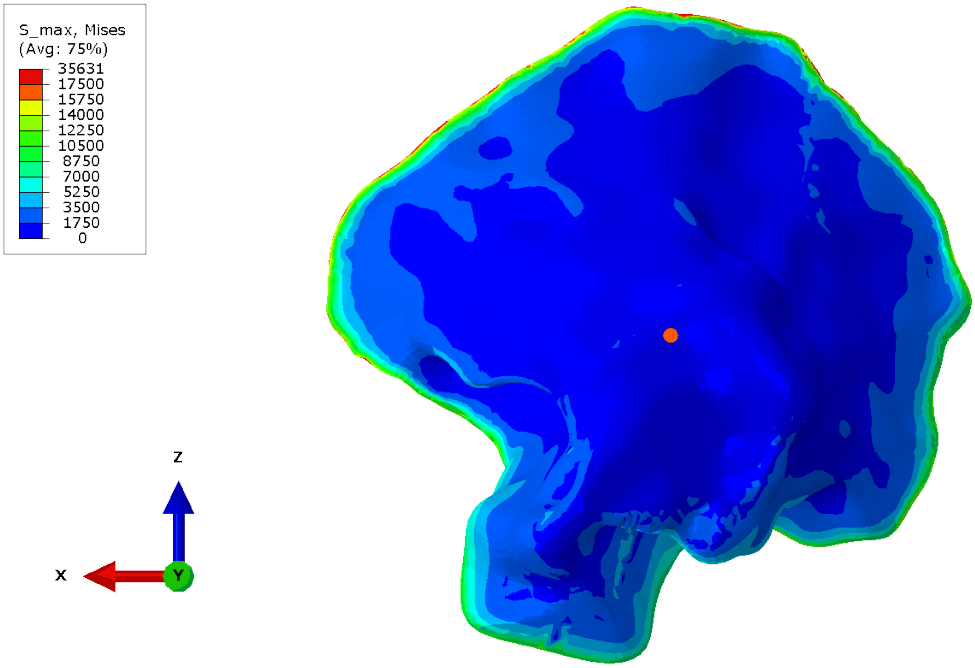

Figure 24. Mises stress (unit: psi) contour on the void surface, overlaid plot from all 8 bending scenarios, end view, with axle centerline location marked.

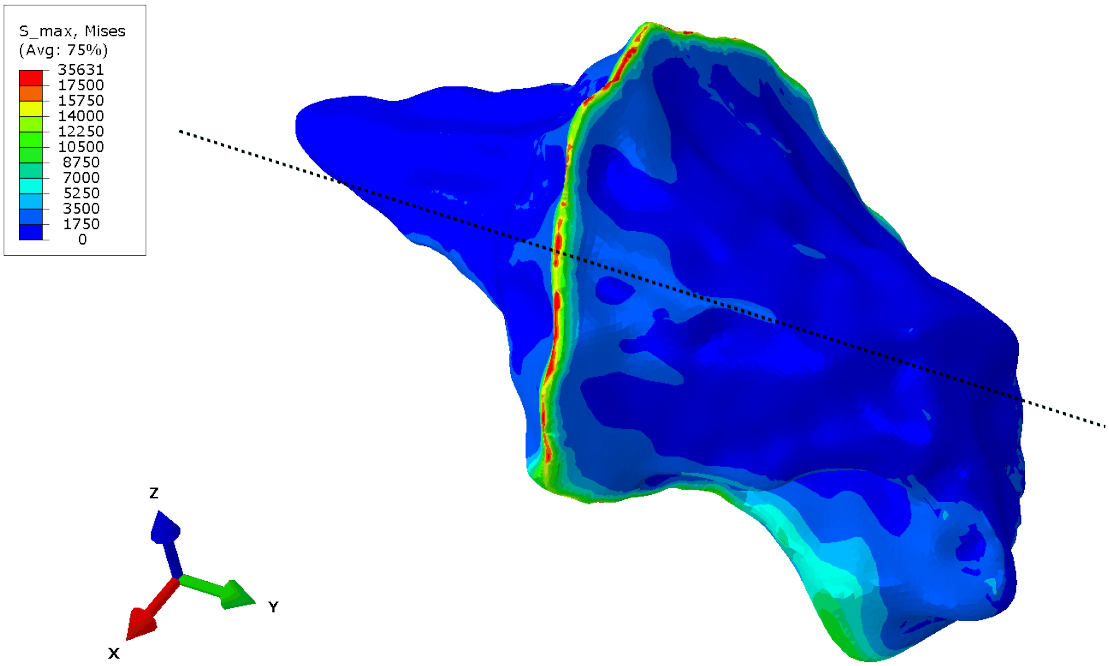

Figure 25. Mises stress (unit: psi) contour on the void surface, overlaid plot from all 8 bending scenarios, isometric view, with axle centerline shown.

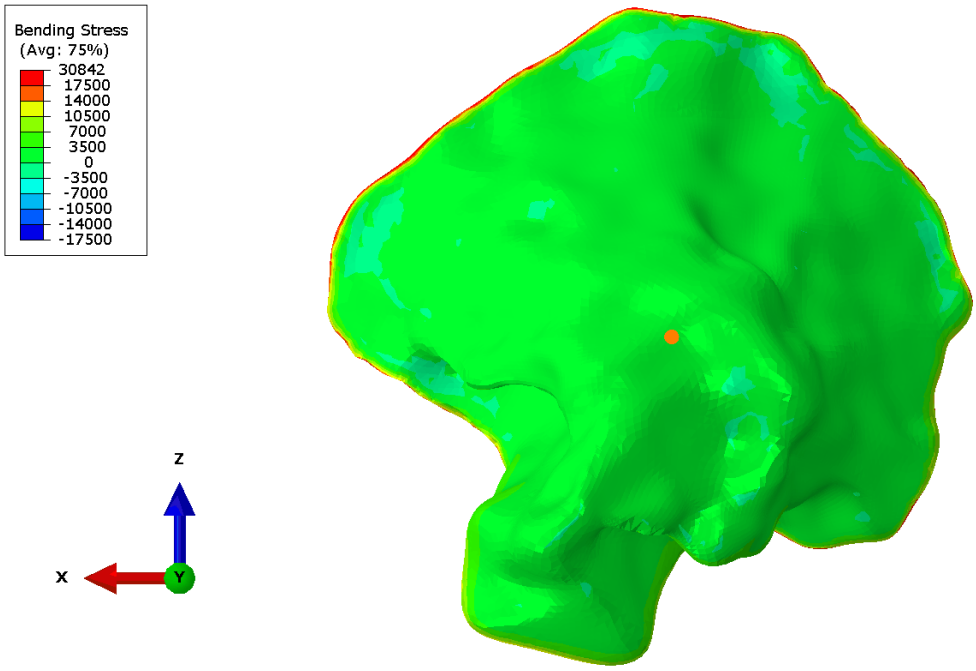

Figure 26. Maximum principal stress (unit: psi) contour on the void surface, overlaid plot from all 8 bending scenarios, end view, with axle centerline location marked.

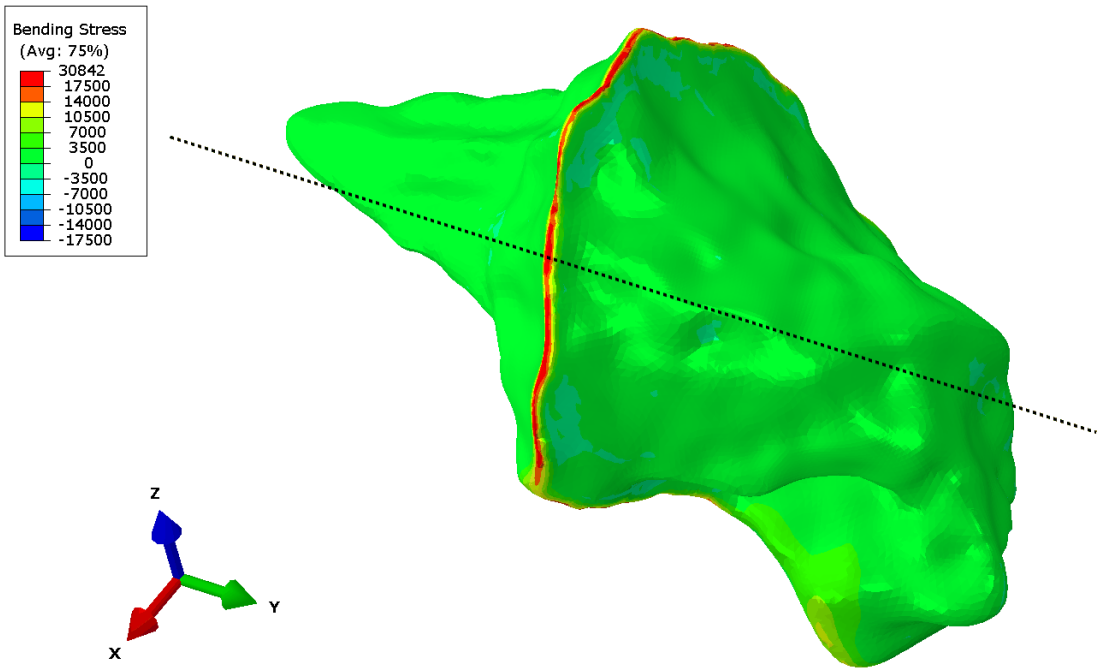

Figure 27. Maximum principal stress (unit: psi) contour on the void surface, overlaid plot from all 8 bending scenarios, isometric view, with axle centerline shown.

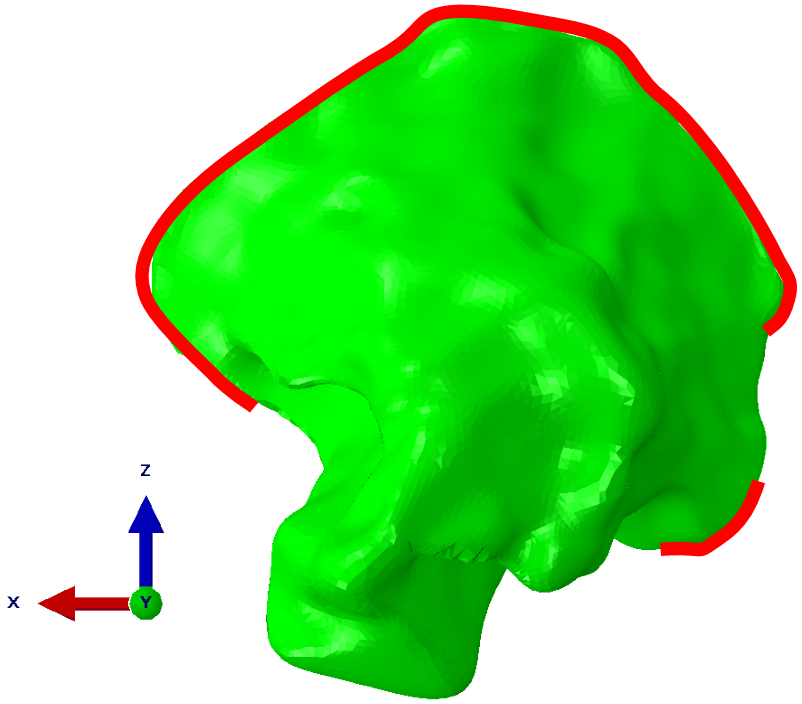

Figure 28. Regions (highlighted in red) on the void surface with high stresses under bending.

Figure 29. Fracture surface of the broken axle with fatigue and overstress areas labeled [Figure 8 of Reference 3].